Low cycle fatigue of additively manufactured thin-walled stainless steel 316L

N.B. When citing this work, cite the original published paper.

(article starts on next page)
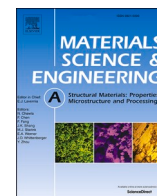
Low cycle fatigue of additively manufactured thin-walled stainless steel 316L

Cheng-Han Yu [a,*], Alexander Leicht [b], Ru Lin Peng [a], Johan Moverare [a]

[a] *Division of Engineering Materials, Department of Management and Engineering, Linköping University, Linköping SE-58183, Sweden*
[b] *Department of Industrial and Materials Science, Chalmers University of Technology, Göteborg SE-41296, Sweden*

ARTICLE INFO

ABSTRACT

To ensure the robust design freedom of metallic additive manufacturing, the fatigue properties and the dimensional limitation of as-built components by laser powder bed fusion (PBF-LB) are investigated. Fully reversed and strain-controlled fatigue tests were carried out on tubular specimens with different wall thicknesses, 1 mm and 2 mm, for the purpose of studying the thin-wall effect without having risk of buckling problem during compression. Two wrought conditions are also enclosed as a comparison, which are the cold worked (CW) and solution annealed condition (SA). In the as-built PBF-LB tubular specimens, deformed microstructure and deformation twins are discovered close to the surface region, together with a higher roughness of the inner surface due to the heat accumulation. The surface roughness is evaluated as micro-notches, and a higher fatigue notch factor, K_f, at lower applied strain range is revealed. The factors influencing K_f include, the non-conductive inclusions serving as crack initiation sites at the surface region, and the deformation twins formed by the local stress concentration. The strain-life of PBF-LB samples is comparable with the wrought samples. However, the fatigue strength of the responding mid-life stress shows greater difference and is in the following order, CW wrought > PBF-LB > SA wrought. Secondary cyclic hardening owing to deformation induced martensitic transformation is found in both of the wrought samples. Yet, only cyclic softening exhibits in the PBF-LB samples, which is the result of the suppressed martensitic transformation and the dislocation unpinning from the cell boundaries.

1. Introduction

Metallic additive manufacturing (AM) is a disruptive technology that can build complex components directly to net shape. The precise energy deposition and material usage make AM more environmentally sustainable compared to traditional manufacturing. Compared to conventional manufacturing techniques, the design freedom from AM also greatly improves customized production. The add-on functionality in various applications include lattice structure for light weight applications [1,2], cooling channel designs within components [3,4], and burner tip repair in gas turbines [5]. Due to the different manufacturing methodologies, the as-built microstructure of AM is different from conventional processes such as casting or forging, and it leads to different mechanical behaviours [6–9]. To establish robust applications of AM and keep the strength of the design freedom, it is necessary to understand the limitation of dimension and the performance of the as-built state. Hence, this study will focus on the fully reversed low cycle

fatigue (LCF) behaviours of AM thin-walled structures, and the material is the stainless steel 316L (SS 316L) manufactured by laser powder bed fusion (PBF-LB).

High surface roughness is commonly found in as-built AM component, and it deteriorates the fatigue performance due to the stress concentration [10–12]. Different surface roughness parameters are in general expected to correlate with fatigue lifetime estimations [13]. Lee et al. [14] has proposed an approach by taking the surface roughness as micro-notches, and using Neuber's rule [15] and Arola–Ramulu model [16] to quantify the surface roughness effect on stress concentrations. The elastic stress concentration factor, K_t, can be mathematically estimated from the surface roughness parameters. However, considering the great ductility of SS 316L, it could show different influence of stress concentrations between the LCF regime and the high cycle fatigue (HCF) regime [17]. Therefore, the fatigue notch factor, K_f, at each applied strain range will be calculated. Besides, the internal defects, such as porosity, lack of fusion and inclusions, have been reported to serve as

stress concentration [12,18–21]. Hence, the mechanisms causing crack initiation will be investigated.

In our previous work, thinner specimens of PBF-LB Ni-based alloy are discovered to show weaker tensile strength due to a texture transition [22]. To address possible thin-wall effects in fatigue behaviours, fatigue specimens with different thicknesses will be implemented in this work. For the purpose of avoiding bulking during the fully reversed low-cycle fatigue testing of thin-walled structures, a tubular fatigue specimen geometry is proposed. Three groups of PBF-LB specimens will be investigated, including the as-built tubular specimens, the tubular specimens with machined and fine polished surface, and the regular cylindrical specimens as a reference. The rough as-built surface can cause large inaccuracy in the determination of load bearing cross section when it comes to thin-walled specimens, leading the uncertainty of responding stress, hence, strain-controlled fatigue tests will be carried out. The influence of the as-built surface state can be investigated by the comparison between the tubular specimens with the two different condition, and the geometry effect can be analysed with the reference of cylindrical specimens.

Cell structure is commonly found in AM materials, and the dislocation interaction with the cell boundaries can improve tensile properties, such as strength and ductility [23–26]. The cyclic response during fatigue of SS 316L correlates to the dislocation structure evolution, for instance, the formation of persistent slip bands (PSB), dislocation cell structure or labyrinth structure, deformation twinning and strain-induced martensitic phase transformation [27–35]. In addition, stacking fault energy (SFE) also greatly governs the deformation mechanisms in austenitic stainless steel [36–42]. Middle range of SFE (20–45 mJ/m^2) can promote deformation twinning and lead to twinning induced plasticity (TWIP), while low range of SFE (<20 mJ/m^2) enhances martensitic phase transformation and yield transformation induced plasticity (TRIP) [43]. For the low cycle fatigue behaviour of SS 316L, a secondary hardening caused by martensitic phase transformation has been reported [33,34,44,45]. However, in view of the possible SFE difference between AM and conventionally manufactured SS 316L [43,46–48], the deformation mechanism could be different. In order to reveal the effects of microstructure and SFE on fatigue behaviour, a wrought SS 316L in the cold worked (CW) state and solution annealed (SA) state will be included as a comparison to PBF-LB SS 316L. The CW state refers to an elongated fine grain structure with high dislocation density that is similar to the PBF-LB microstructure, while the SA state greatly lowers the dislocation density and the amount of grain boundaries.

2. Experiments

2.1. Laser powder bed fusion process

An inert gas-atomized SS 316L powder with a size distribution of 20–53 μm was used as a feedstock material, where the chemical composition of the powder is provided in Table 1. Note that the chemical composition was determined by using inductively coupled plasma-optical emission spectrometry (ICP-OES); for the interstitial element analysis, combustion gas analysis was applied for the carbon and sulphur content, and hot fusion analysis was employed for the oxygen and nitrogen content. The samples were fabricated in an EOS M290 machine equipped with an Yb-fiber laser with a maximum nominal power of 400 W and laser spot diameter of approximately 100 μm. The build chamber was flushed with high-purity argon gas to retain the oxygen content in the build chamber at below 0.1%. The samples were

produced by using a 20 μm layer thickness and standard process parameters (version 1.10) developed for SS 316L by EOS GmbH. Furthermore, a pre-defined scan strategy known as stripe scanning, in which a 67° scan rotation is performed after each layer. All fatigue specimens were built vertically along the building direction (BD) where the loading direction is parallel to the BD. All the samples were printed in the same batch to avoid any possible difference between batches, such as oxide layer difference between different time of powder recycling.

2.2. Fatigue tests

Fully reversed uniaxial low cycle fatigue (LCF) tests were carried out on three studied groups of PBF-LB SS 316L at room temperature under strain-control. An axial extensometer with a gauge length of 12.5 mm has been used for strain measurements. The LCF tests followed the standard ISO 12106, and a servo hydraulic fatigue test rig was applied with an Instron 8800 controller and an Instron ±50 kN load cell. The aim of this study was to investigate the influence of thin-wall effects and the as-built rough surface on LCF properties, hence, tubular fatigue specimens with 1 mm and 2 mm wall thickness were produced. One group of the tubular fatigue specimens were tested at the as-built state with rough surface resulting from the PBF-LB process, which is labelled as AB_1 mm and AB_2 mm. The specimen geometry of AB_1 mm is shown in Fig. 1, where the BD and radial direction (RD) are given. The second group were tests on tubular specimens with machined and fine polished surface, which is labelled as M_1 mm and M_2 mm. This group of specimens was built with an extra 100 μm added to both inner and outer sides of the wall to give space for the post surface-processing. The outer radius of both groups was fixed as 5 mm, and the inner radius was 4 mm and 3 mm respectively for the two different wall thicknesses. The third group was cylindrical specimens machined from as-built rods with a diameter of 15 mm, which serve as a reference group for PBF-LB SS 316L, and is labelled as AB_rod. The purpose of testing AB_rod is to address the geometrical effect of the tubular fatigue specimens. The radius of the gauge length was 3 mm, and the surfaces were machined and fine polished. The parallel length of all three groups of specimens was 15 mm.

The LCF tests described above were also performed on two different groups of wrought SS 316L as a comparison between PBF-LB and conventional manufacturing. The specimen geometry and surface condition are the same as for the AB_rod samples. The as-received bar (diameter of 16 mm) of wrought SS 316L was in "Hot rolled – Annealed Cold Drawn" condition according to ISO 10474 (2013), and is referred as Wrought_CW. Additional fatigue specimens have been subjected to a solution annealing heat treatment at 1060 °C for 30 min followed by
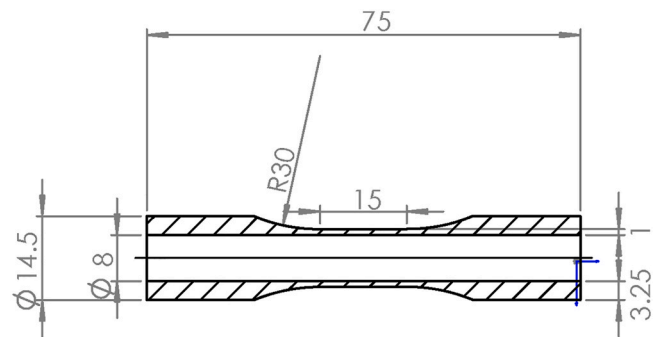

Fig. 1. Fatigue specimen geometry of AB_1 mm.

Table 1
The chemical composition of the powder.

Element	Fe	C	Cr	Mn	Mo	N	Ni	O	P	S	Si
Wt.%	Bal.	0.009	17.4	1.6	2.7	0.06	13.4	0.04	0.006	0.005	0.3

water quenching, and they are defined as the group of Wrought_SA samples. The chemical composition is given in Table 2.

In brief, three groups of as-built tubular fatigue specimens with different surface condition have been examined, and they are compared with cold worked and solution annealed wrought samples. The different groups of specimens are summarized in Table 3.

2.3. Micro computed tomography and surface roughness analysis

Micro computed tomography (μCT) scans were applied on the gauge section of the tubular fatigue specimens with as-built surface condition. The μCT scans were performed by using a commercial CT scanner GE V| Tome|X 180/300 (GE Sensing & Inspection Technologies GmbH, Wunstorf, Germany) with a source of 300 kV. A voltage of 200 kV and a current of 50 μA in combination with a silver prefilter of 0.25 mm thickness were applied. For each projection, it was the average of 3 measurements with an exposure time of 3 s for each, and 2100 projections in total were acquired for each specimen. A voxel size of 10 μm^3 was achieved.

The surface roughness was investigated by using image analysis on the multiple cross sections from the μCT scans. An in-house MATLAB script was applied for the image analysis [49], and the surface roughness was determined along the loading direction. A schematic roughness profile for the image analysis is shown in Fig. 2, and the different roughness parameters are determined as follow, R_a (arithmetic mean values of the Z-coordinates), R_c (mean value of Zt_i in each S_i), R_z (maximum Zt_i), R_v (maximum Zv_i), R_p (mean value of Zp_i in each S_i) and R_q (root mean square of the Z-coordinates) [22].

2.4. Microstructure analysis

The cross-section of interest was prepared by using electrical discharge machining. The cross-section was first polished from 500 Grit up to 400 Grit, and then was applied to the fine polishing with diamond suspension from 3 μm down to 0.25 μm. The OP-U colloidal silicon suspension was used as the final polishing step followed by using the water to remove the residual particle from the suspension.

The microstructure and fractography were studied by using a Hitachi SU 70 field emission scanning electron microscope (FE-SEM), and both backscattered and secondary electron imaging have been applied. The grain orientation maps were analysed by using an Oxford EBSD (Electron backscatter diffraction) detector. The step sizes were chosen differently between 0.1 μm and 1 μm depending on the magnification.

The dislocation structure of fatigued specimen was investigated by using a transmission electron microscope (TEM), FEI Tecnai G2, which was operated at an acceleration voltage of 200 kV. A slice of the gauge section was manually ground to a TEM thin foil, and the final polishing was carried out by using a Struers twin-jet electropolishing system with the following conditions, at the temperature of −25 °C, the applied voltage of 22.5 V, and the electrolyte of 10% perchloric acid with 90% ethanol.

3. Results

3.1. Surface roughness

The outer and inner surfaces of the tubular specimen obtained by μCT are shown in Fig. 3. The spherical features are shown on both sides of the surfaces, which are the semi-melted or unmelted powders, and they will also be identified by the grain orientation maps in the next

Table 3
Summary of different groups of fatigue specimens.

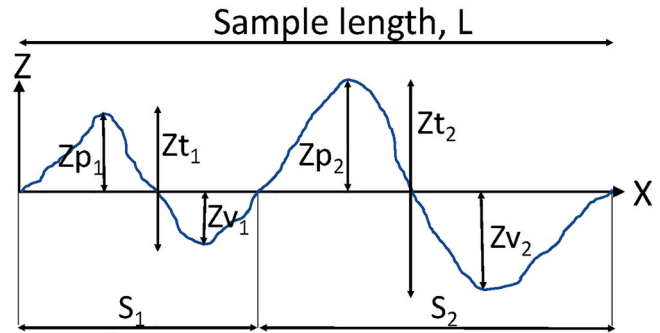| Group	Process	Surface condition	Heat treatment
AB_1 mm & AB_2 mm	PBF-LB	As-built surface	None
M_1 mm & M_2 mm	PBF-LB	Machined & fine polished	None
AB_rod	PBF-LB	Machined & fine polished	None
Wrought_CW	Wrought	Machined & fine polished	Hot rolled – Annealed Cold Drawn
Wrought_SA	Wrought	Machined & fine polished	Solution annealed

Fig. 2. *The roughness profile for parameter determination* [22].

section. The inner surface exhibits more spherical semi-melted or unmelted powders attaching and sitting on the top of each other, which can possibly increase the height variation of the roughness profile and lead to higher surface roughness. The analysed surface roughness is shown in Table 4. In general, all the roughness parameters of the inner surface are much higher than the outer surface, and the roughness of the specimen with 1 mm wall thickness is slightly higher than the 2 mm one. The roughness difference between the inner and outer surface correlates well with the observation in Fig. 3. An addition information from μCT scanning is that the specimens are fully dense and nearly porosity free.

3.2. Microstructure

3.2.1. PBF-LB SS 316L

The as-built microstructure from different cross-sections of AB_1 mm are shown in Fig. 4(a) and (b). Roughly equiaxed grain structure is found from the top view, and elongated grain structure is discovered from the side-view. The grain size determined from the top view is 17 ± 16.4 μm. As the colour legend is along the BD, the majority of the columnar grains are identified as having the texture component <011>//BD (green colour), meanwhile, the smaller grains in between are either <001>// BD or random texture. Within the columnar grains, cell structure can be found and indicated by low angle grain boundaries. A further zoom-in on the cell structure is shown in Fig. 5 where the dislocation structure is revealed by using STEM. High dislocation density is found at the cell boundaries, and the size of the cell structure is around 300–500 nm in diameter.

Tiny grains are discovered at the surface of both sides, and it is relatively more thin and elongated grains close to the inner surface side. A closer look at the inner surface region is shown in Fig. 4(c)–(f), where four different maps are given. Compared to the uniform microstructure

Table 2
Chemical composition of the wrought SS 316L. The composition is according to the certification from the material supplier.

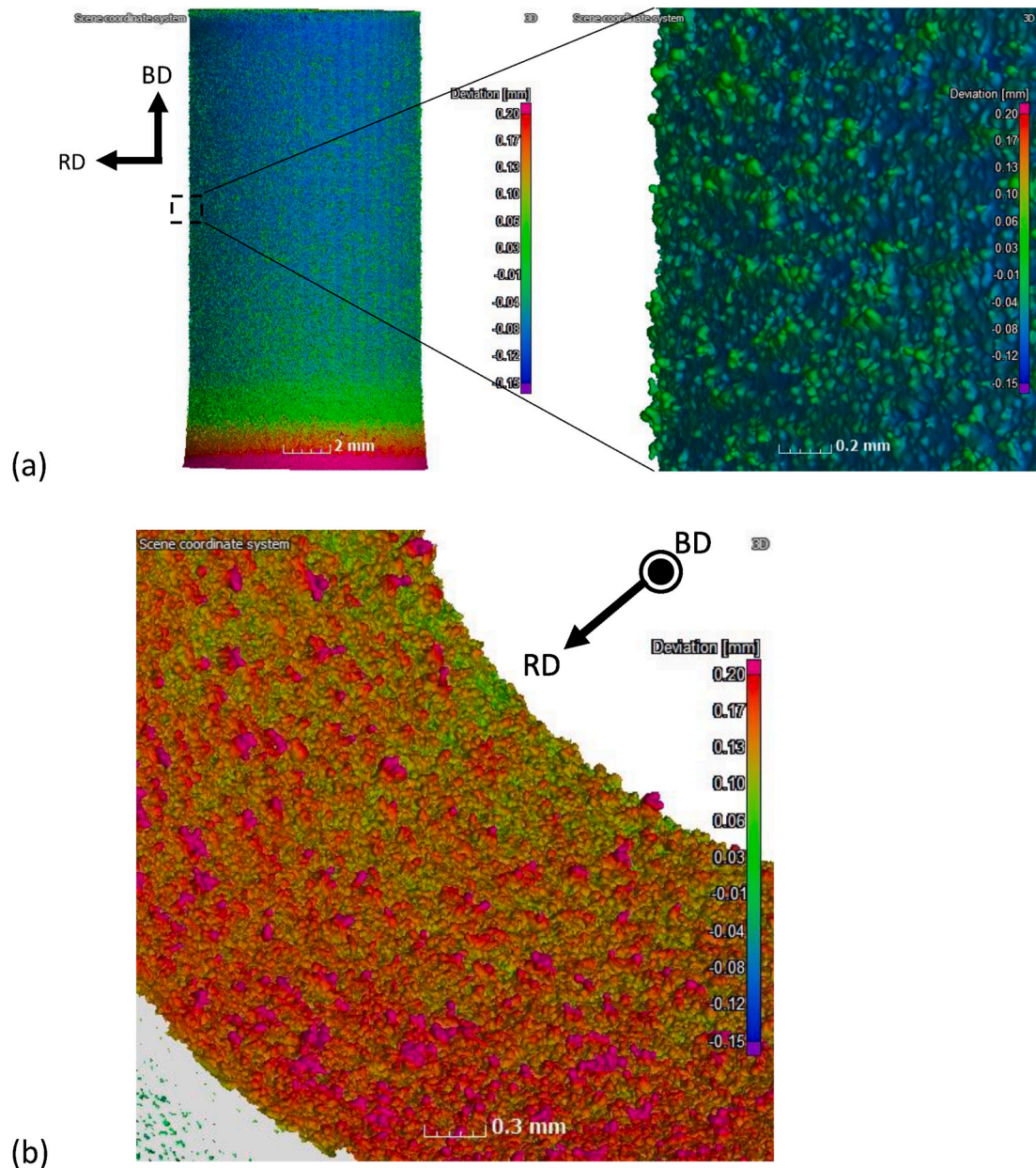| Element	Fe	C	Cr	Mn	Mo	N	Ni	P	S	Si
Wt.%	Bal.	0.01	16.87	1.51	2.04	0.058	10.16	0.028	0.026	0.47

Fig. 3. Reconstructed 3D images from μCT scans of the gauge section of AB_2 mm. (a) The outer surface. (b) The inner surface.

Table 4
Surface roughness analysis on the gauge section of the tubular fatigue specimens.

Wall thickness	1 mm	1 mm	2 mm	2 mm
	Inner surface	Outer surface	Inner surface	Outer surface
Rp (μm)	69.1	44.0	60.6	40.3
Rv (μm)	47.5	24.1	41.8	25.4
Rz (μm)	116.6	68.1	102.3	65.7
Rc (μm)	71.4	38.1	65.3	40.9
Ra (μm)	19.1	11.0	17.8	10.9

in the bulk region, a finer but more inhomogeneous grain structure is found in a surface layer of around 100–200 μm (Fig. 4(c)). Further, the layer is plastically deformed, as shown in Fig. 4(f), and deformation twins are also discovered close to the outer surface regime, see Fig. 4(e). Though the microstructure is inhomogeneous close to the inner surface, it is still fully austenitic, see Fig. 4(d).

3.2.2. Wrought SS 316L

The microstructures of the reference group, Wrought_CW and Wrought_SA, are shown in Fig. 6, where finer grain structure is revealed in Wrought_CW. The grain size of Wrought_CW is 25 ± 18.8 μm, and the grain size of Wrought_SA is 38.9 ± 24 μm. One can find more low angle grain boundaries in Wrought_CW, which indicates that there are more finer grains within the grains determined by high angle grain boundaries and possibly higher dislocation density. In addition, annealing twins are found in both samples, and the volume fraction is much higher than PBF-LB SS 316L.

3.3. Fatigue results

The strain-life fatigue results are shown in Fig. 7(a) in a logarithmic scale. In the high strain range regime, the lifetime of all groups is at the same level, but a larger difference is observed at lower strain ranges. For each test condition, the total strain is composed of elastic strain and plastic strain, which can be determined from the hysteresis loop. The
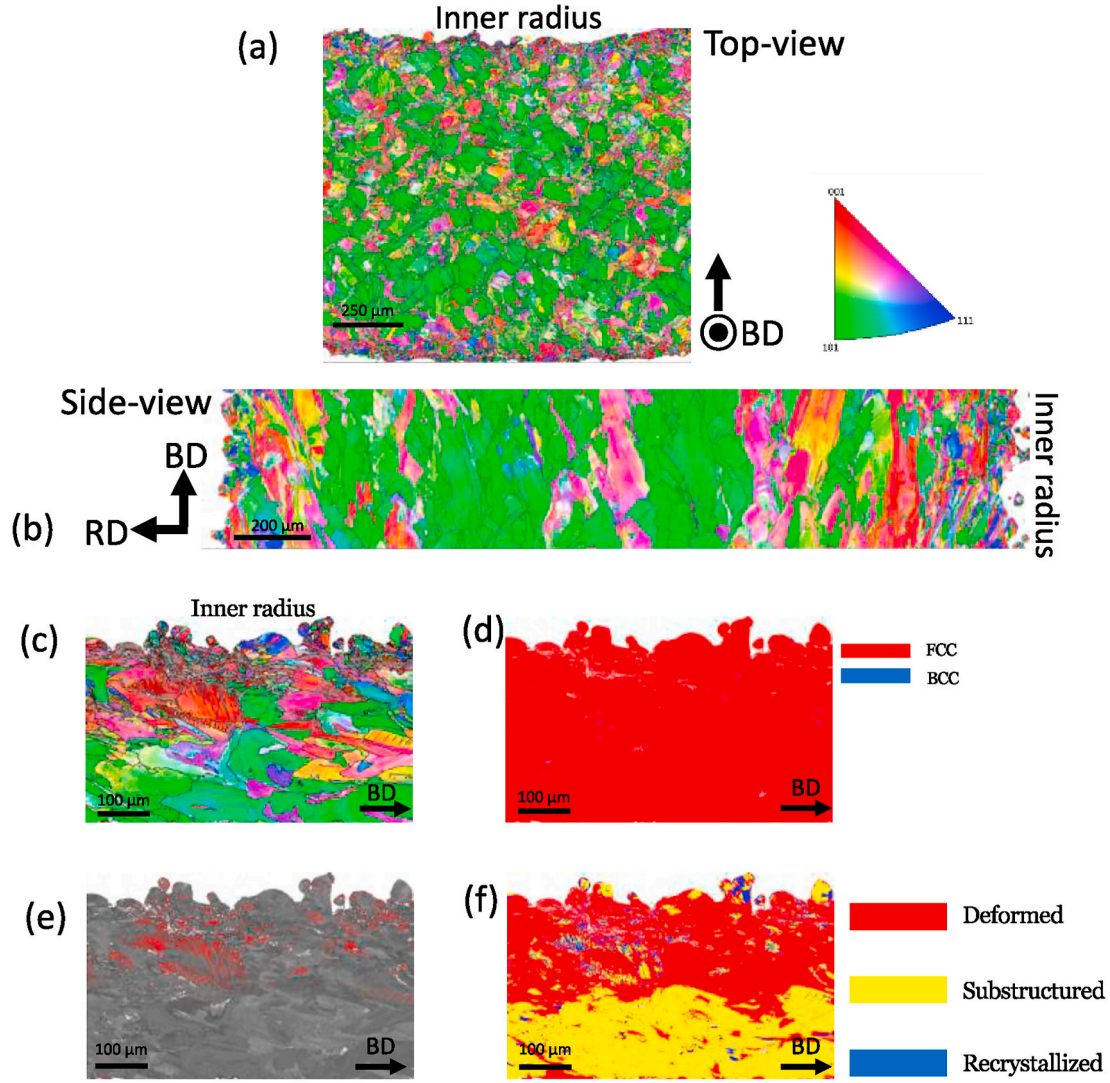
Fig. 4. EBSD grain orientation mapping of the as-built microstructure of AB_1 mm. High angle grain boundaries (>10°) are labelled by the thick black lines, and the low angle grain boundaries (>2°) are labelled by the thin grey lines. The colour legend of each grain orientation map is corresponding to the BD. (a) The top view where the inner surface is at the upper side. (b) The side view where the inner surface is at the right side. (c)–(f) are the microstructure at the inner surface region. (c) Grain orientation map. (d) Phases map. (e) Band contrast map. The deformation twins are labelled by the red lines. (f) Recrystallization fraction map, which is determined by the misorientation between each grain. (For interpretation of the references to colour in this figure legend, the reader is referred to the Web version of this article.)

relation between fatigue-life and total strain amplitude can be described by two parts, the elastic strain-life relation given by Basquin's equation, and the plastic strain-life relation characterized by Coffin-Manson's equation [13,50]. The elastic strain can be calculated from the measured mid-life stress amplitude and E by using Hook's law. The combined equation is shown as follows,

$$\frac{\Delta\varepsilon}{2} = \varepsilon_a = \frac{\Delta\varepsilon_e}{2} + \frac{\Delta\varepsilon_p}{2} = \frac{\sigma_f'}{E}(2N_f)^b + \varepsilon_f'(2N_f)^c \qquad (1)$$

where ε_a is the strain amplitude, $\Delta\varepsilon_e$ and $\Delta\varepsilon_p$ are the mid-life elastic and plastic strain amplitude respectively, σ_f' is the fatigue strength coefficient, ε_f' is fatigue ductility coefficient, b and c are curve fitting exponents respectively, E is the Young's modulus, and N_f is the total fatigue life at failure. The life cycle numbers, at which the elastic strain and plastic strain are equal, is defined as the transition fatigue life, N_t. N_t typically separates the LCF and HCF regime, where elastic strain dominates in HCF regime and plastic strain dominates LCF regime. The fatigue life estimation parameters above are listed in Table 5. Note that the

fitted ε_f' and c of AB_1 mm and AB_2 mm shows large deviation from the other groups, which is assumed to be caused by the surface condition, and it will be discussed in section 4.2.

A surface roughness calibration method has been proposed in our previous work [22], which states that the overestimated cross-section due to the roughness should be subtracted by roughness parameter Rp to obtain a more accurate stress value, see the definition of Rp in Fig. 2 in section 2.3. This roughness calibration method has also been applied on AB_1 mm and AB_2 mm to obtain the responding stress, where the inner and outer surfaces have been calibrated with its own roughness value. The outer radius of the tube was measured directly by callipers, and the inner radius was determined by examining the CT scans.

In Fig. 7(b), the responding stress of each applied strain range is determined at the mid-life, and the stress-life fatigue results are plotted. The Wrought_CW and the Wrought_SA are the best and the worst fatigue lifetime respectively, and the fatigue lifetime of PBF-LB samples stands in between. In stress-life, the ranking of fatigue lifetime among the PBF-LB samples is similar to the strain-life. However, the lowest points of the stress range of AB_1 mm and AB_2 mm show large deviation to the
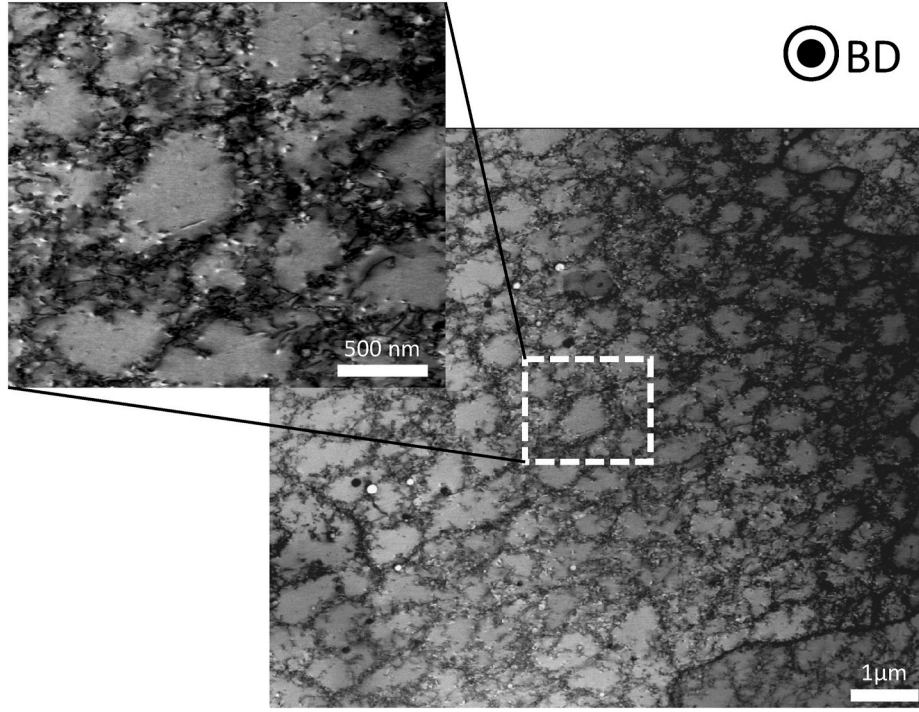
Fig. 5. Dislocation structure of the as-built PBF-LB SS 316L imaged by using STEM.
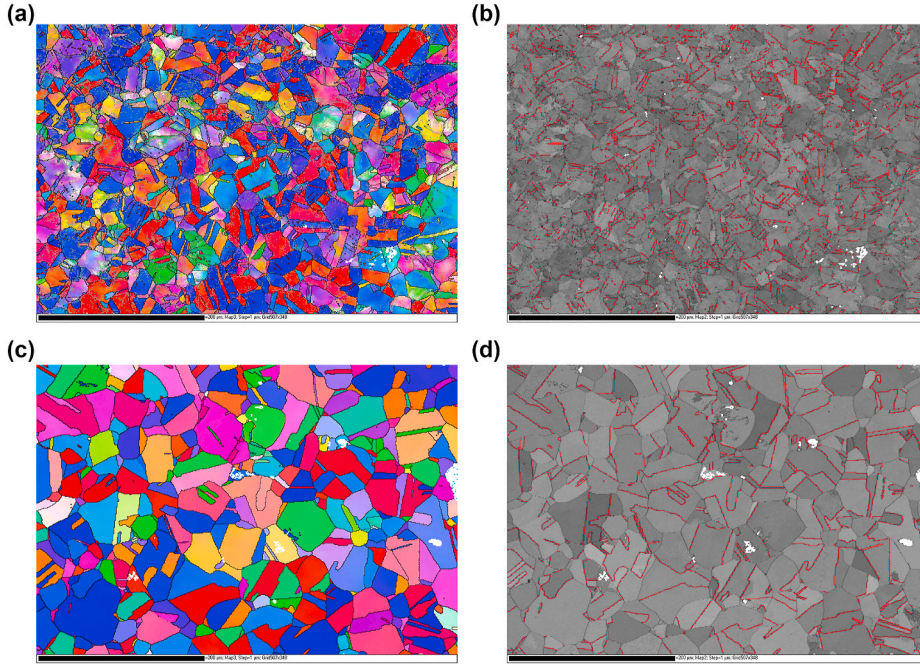

Fig. 6. EBSD grain orientation mapping of the wrought SS 316L, where the loading direction is out-plane. (a) and (b) are from Wrought_CW. (c) and (d) are from Wrought_SA. For (a) and (c), the high angle grain boundaries (>10°) are labelled by the black lines, and the low angle grain boundaries (>2°) are labelled by the grey lines; the colour legend refer to the loading direction. For (b) and (d), both are images from band contrast with the Σ3 {112} incoherent twin boundaries labelled by the red lines. (For interpretation of the references to colour in this figure legend, the reader is referred to the Web version of this article.)

trendline, which is the result of the shorter lifetime at lower applied strain range. In Fig. 7(c), the cyclic stress-strain curves are fitted based on the Ramberg-Osgood relation, where the equation is given as follows [51],

$$\varepsilon_a = \varepsilon_e + \varepsilon_p = \frac{\sigma_a}{E} + \left(\frac{\sigma_a}{H'}\right)^{\frac{1}{n'}} \tag{2}$$

ε_a is the strain amplitude, ε_e is the elastic part and ε_p is the plastic part of the strain amplitude, σ_a is the mid-life stress amplitude, E is the young's modulus, H′ is the cyclic strength coefficient and n′ is the strain

hardening exponent. The fitted parameters are listed in Table 5. A monotonic tensile stress-strain curve of PBF-LB SS 316L is also included in the figure.

3.4. Fractography

The fractography of the different groups of samples are shown in Fig. 8. In general, multiple crack initiation and propagation sites are found in each group. Moreover, non-conductive inclusions with various shapes can be found close to the surface regions, and they are assumed to
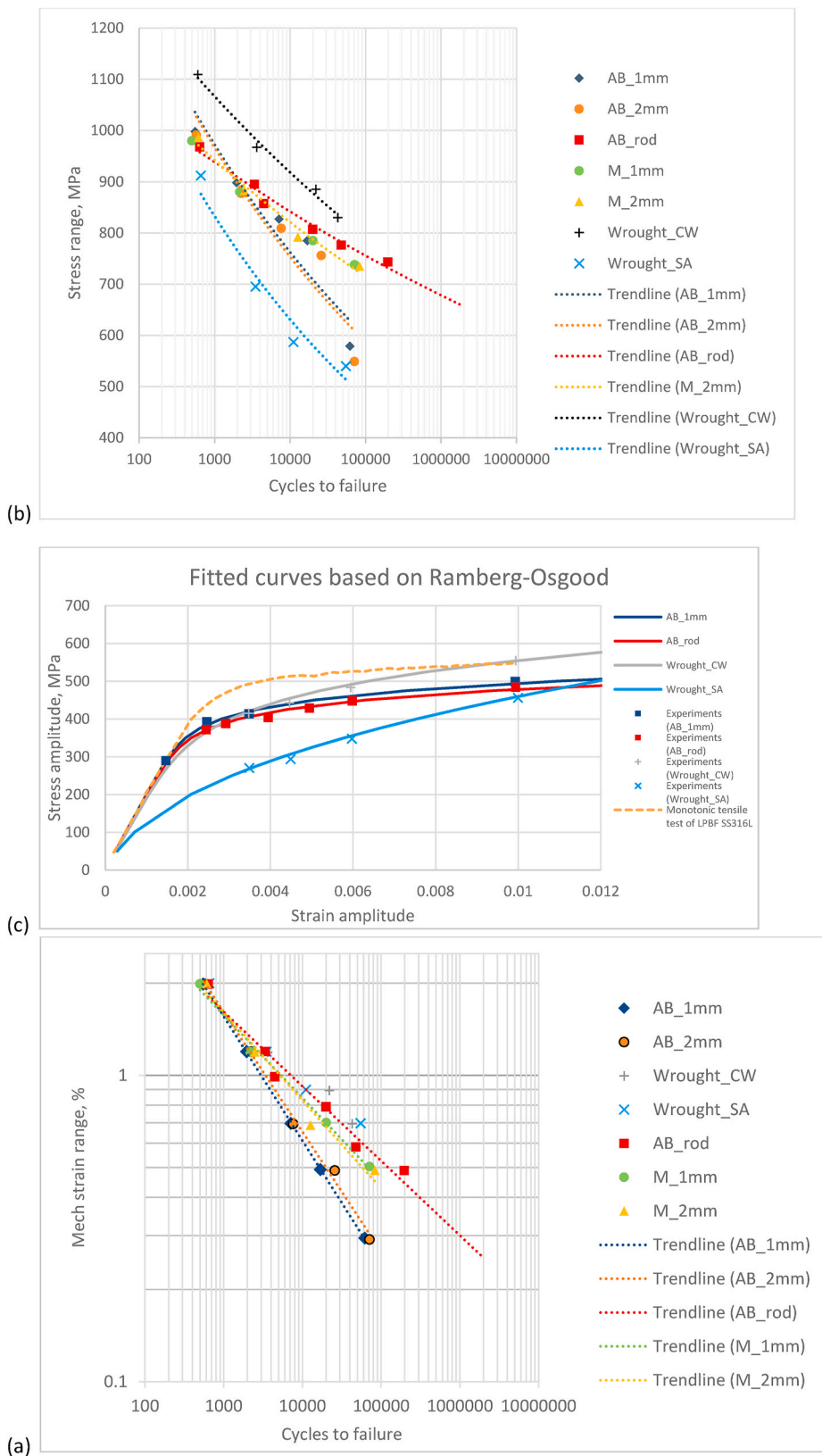
Fig. 7. (a) The applied strain range versus lifetime. Note that it is in log-log plot. (b) The mid-life stress range versus lifetime, where the responding stress range is determined at the mid-life of each applied strain range. Note that the cycle is in log scale. (c) The cyclic stress-strain curves fitted from the Ramberg-Osgood relation, and the experimental results of the applied strain and responding stress are included along the curves. The stress-strain curve of monotonic tensile test is obtained from the first tensile loading cycle of the fatigue test. Note that the trendlines are fitted by using power-law function.

be the crack initiation points. The conductivity of the inclusion is quite different from the major component, hence, the inclusions can be clearly indicated by the imaging contrast.

For AB_1 mm, the fracture surfaces close to the surface area and in the centre of the bulk are shown in Fig. 8(a)–(d). The valley of the rough surface and the non-conductive inclusions serve as cracking initiation points from the surface. In the bulk region, the serration and different crack propagation directions are revealed. For the fracture surfaces of M_1 mm shown in Fig. 8(e)–(f), the crack initiations are also from the non-conductive inclusions that are embedded at the surface region even

Table 5

The fitted parameters from Basquin's and Coffin-Manson's law for elastic and plastic strain-life relation. The fitted parameters for stress-strain curve from Ramberg-Osgood relation. The parameter fitting is based on the data points of the LCF results shown in Fig. 7a.

Sample Label	Basquin's and Coffin-Manson's law					Young's Modulus	Ramberg-Osgood	
	σ_f'	b	ε_f'	c	Nt		H'	n'
AB_1 mm[a]	1085.3	−0.106	29.262	−1.109	2675	200.5	789.11	0.0956
AB_2 mm[a]	1099.7	−0.108	40.436	−1.135	2895	200	768.2	0.0945
M_1 mm	714.95	−0.056	0.2413	−0.503	5669	192.3	827.5	0.1099
M_2 mm	743.47	−0.06	0.3339	−0.539	5637	194.4	840.78	0.1115
AB_rod	669.11	−0.047	0.2212	−0.475	8545	196	769.62	0.0972
Wrought_CW	874.01	−0.065	0.1125	−0.396	8099	192.2	1239.5	0.1626
Wrought_SA	1040	−0.12	0.0555	−0.29	545854	199.2	3572.5	0.4214

[a] Note that the fitting parameters for these samples are highly influenced by the surface roughness and therefore deviates strongly from commonly seen values.

though the rough surface has been properly removed. For the fracture surface of AB_rod shown in Fig. 8(g)–(h), three major cracks propagate from the surface, and the non-conductive inclusions serve as the crack initiation as well. In addition, no significant defects are found in the bulk region of each group, which is assumed to be related to the fully dense and nearly defect free of the specimens as confirmed by μCT scanning.

4. Discussion

4.1. Influence of microstructure and surface roughness on fatigue lifetime

The as-built microstructure of tubular specimen shown in Fig. 4 shares the similarity with other PBF-LB stainless steel [47,52,53] and materials with FCC phase [26,54,55]. The cell structure, high dislocation density and dislocation piling up at grain boundaries are hypothesized to be features existing in the as-built microstructure as reported in the literature [23,25]. On the other hand, the cold drawn process of wrought SS 316L can lead to elongated grain structure, grain refinement, and high dislocation density, which resemble the microstructure in PBF-LB SS 316L. As a result, the fatigue performance of AB_rod can be comparable with the Wrought_CW, particularly in the regime of low applied strain range as illustrated by the trendline shown for the stress-life in Fig. 7(b), and also the similar N_t values shown in Table 5. In addition, the cell structure of PBF-LB SS 316L is assumed to be beneficial for the fatigue resistance [17]. Considering that the solution annealing lowers the dislocation density and the amount of grain boundaries, the fatigue strength turns out to be lower than for the PBF-LB ones.

For the tubular specimens, both AB_1 mm and AB_2 mm show higher surface roughness for the inner surface side than the outer surface side, and it is presumed to be caused by the higher heat accumulation in a close loop. The heat accumulation sinters more powders to the surface, which makes the powders stand on top of each other and induce higher roughness. However, it is surmised that the higher surface roughness does not increase the stress concentration significantly at the inner surface since the part of increased roughness is away from the load bearing region. Surface cracks from specimens fatigued in the highest and lowest applied strain ranges respectively are shown in Fig. 9. Transgranular crack propagation is discovered in both cases. The cracks are found to be close to the valley part of the roughness surface, and secondary cracks are revealed. Yet, some different microstructural responses between the two applied strain range also exhibits. For the strain range of 2%, it exhibits highly deformed microstructure along the major crack, and deformation twins are discovered at the deformed regime. Since it is a fully reverse fatigue test, the compression process highly contributes to the plastic zone. For the strain range of 0.3%, the plastic deformation accompanied by twinning is only observed at the crack tip, see Fig. 9(e), and the deformation twins at the crack tip are assumed to be beneficial to hinder the crack propagation. The deformation twins correlate with the local stress concentration and play a role in the plasticity.

From the fracture surfaces shown in Fig. 8 it can be seen that non-

conductive inclusions initiates cracks at the surface area in all the three groups. Such inclusions have also been found in other fatigue studies of PBF-LB materials and have been reported to trigger crack initiation [19–21]. There is a difficulty to characterize the composition of non-conductive inclusions since they stand on the fracture surface, but it is presumed to be the inclusion formed from the contamination in the chamber during the printing process. Considering that the surface region is a relatively weaker point compared to the bulk region due to the surface roughness and the potential defects, the larger surface area could lead to lower fatigue life. Therefore, the fatigue life of M_1 mm and M_2 mm are lower than AB_rod as a result of the larger surface area/-volume ratio, even though the surface has been machined and fine polished. On the other hand, the fatigue life difference of the tubular specimens with machined and as-built rough surface is obviously caused by the high surface roughness and the stress concentration at the valley part of the roughness profile. The fatigue performance is sensitive to the surface condition, and it has an impact on the transition fatigue life where the N_t of as-built surfaces is the lowest among the different groups. For the same number of cycles to failure, the specimens with a rough surface experience less amount of nominal plastic strain, and the plastic strain is assumed to be localized to the stress concentrations and causing the multiple crack initiation points. Hence, the fitted parameters from Coffin-Manson's law for AB_1 mm and AB_2 mm also shows large deviation from the other groups.

4.2. Fatigue notch factor

To quantify the stress concentration of the as-built rough surface, the surface roughness is evaluated as micro-notches on the surface [14,16], and the fatigue notch factor (K_f) will be calculated by using Neuber's rule [13,15]. As shown in Fig. 9, it is common to find the valley part of surface roughness as crack initiation point due to the stress concentration. The radius of the valley plays a critical role on K_f [16,56], and this approach has been applied to quantifying the stress concentration of machined surfaces with a fairly constant roughness. However, it is a relatively larger variation of the roughness profile for PBF-LB as-built surfaces than machined surfaces, but the K_f value calculated in the later part of this work represent the surface effect from the whole gauge length of the sample and takes both the inner and outer surface into account.

For the same strain range that has been applied to both as-built and machined surfaces of the tubular specimens, the K_f can be calculated by comparing the two groups. It requires the lifetime estimation from Equation (1), the fitted curves from Ramberg Osgood relation in Equation (2), and Neuber's rule shown in Equation (3) [15],

$$\Delta\sigma \times \Delta\varepsilon = \Delta S \times \Delta e \times k_f^2 \tag{3}$$

where $\Delta\sigma$ and $\Delta\varepsilon$ are the local stress and strain, Δe is the applied strain range, ΔS is the responded stress range, and K_f is the fatigue notch factor. Since there is an uncertainty of responding stress of tubular specimens with rough surface, the stress will be estimated from the cyclic stress-
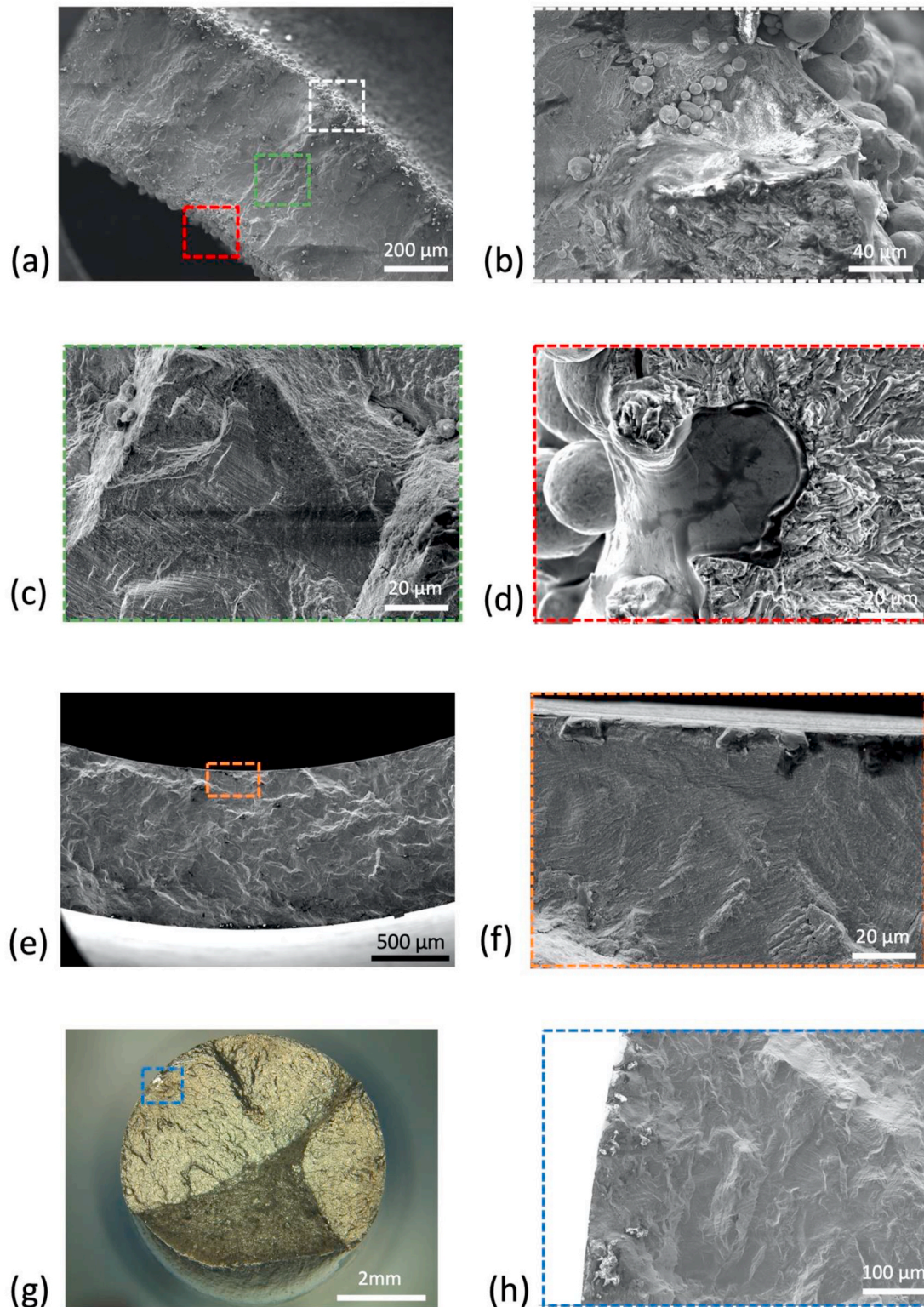
Fig. 8. Fractography of the three different groups at the regime of low applied strain range. Note that (g) was imaged by light optical microscope, and the rest were imaged by secondary electrons in SEM. (a)–(d) are from AB_1 mm at the strain range of 0.3%. (b) The white labelled area in (a), showing the non-conductive inclusions at the outer surface region. (c) The green labelled area in (a), showing the fatigue serration at the bulk region. (d) The red labelled area in (a), showing non-conductive inclusions at the inner surface region. (e)–(f) are from M_1 mm at the strain range of 0.5%, where the orange labelled area is shown in (f). (g)–(h) are from AB_rod at the strain range of 0.5%, where the blue labelled area is shown in (h). (For interpretation of the references to colour in this figure legend, the reader is referred to the Web version of this article.)
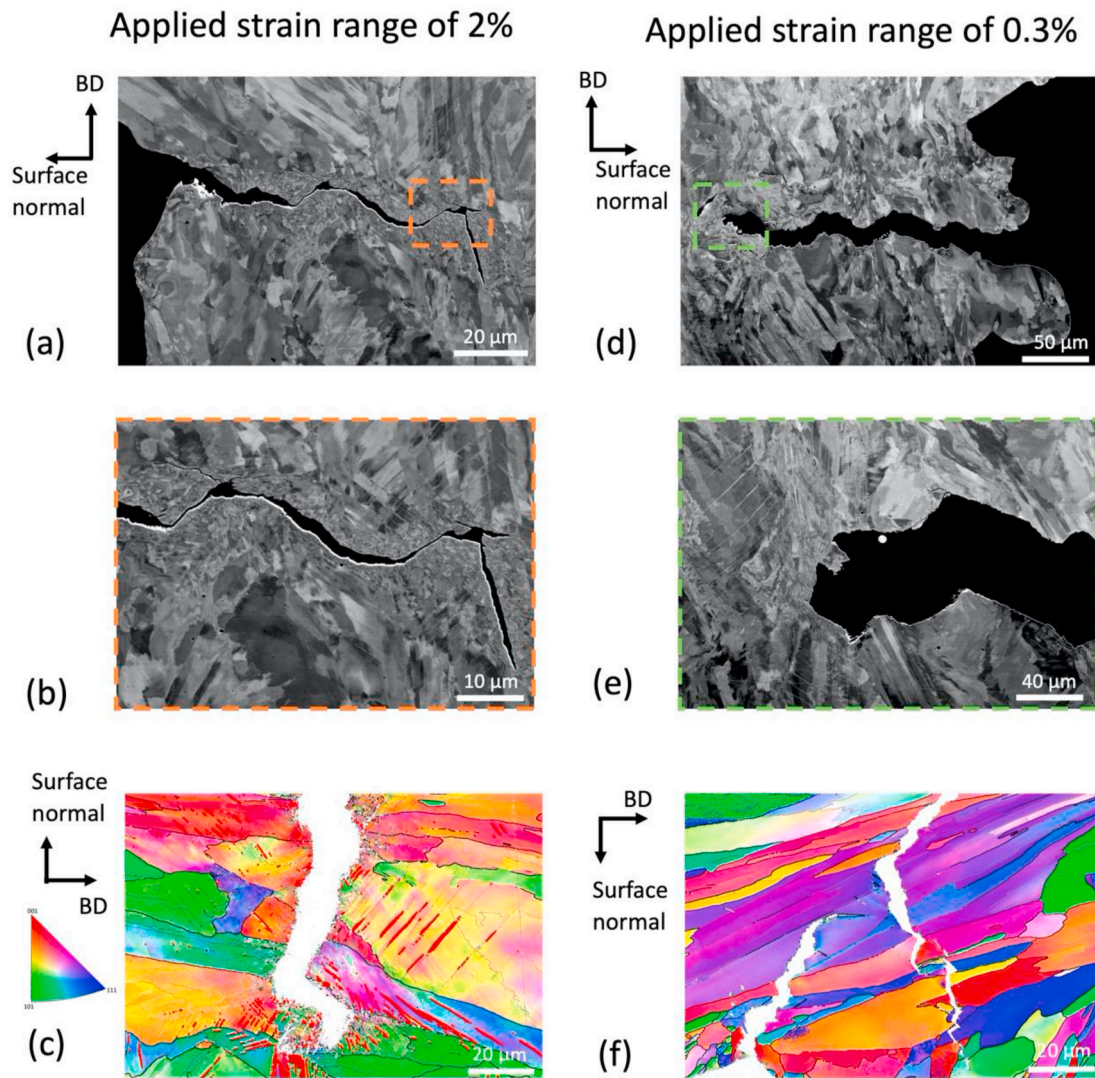
Applied strain range of 2%

(a)

(b)

(c)

Applied strain range of 0.3%

(d)

(e)

(f)

Fig. 9. Crack propagation of AB_1 mm at different strain range, which is taken from the fatigued specimens that are at failure. (a)–(c) are from the strain range of 2%; the regime of the crack tip in (a) labelled in orange is shown in (b), and (c) is from another area. (d)–(f) are from the strain range of 0.3%; the regime of the crack tip in (d) labelled in green is shown in (e), and (f) is from another area. Note that (a), (b), (d), (e) are backscattered SEM images; (c) and (f) are EBSD images, where the colour legend refers to the BD, and the deformation twins are indicated by the red lines. (For interpretation of the references to colour in this figure legend, the reader is referred to the Web version of this article.)

strain curve of the tubular specimen with machined surface. Take AB_1 mm and M_1 mm as an example. First, the local strain $\Delta\varepsilon$ is calculated by using Equation (1) and taking the lifetime of AB_1 mm as input. Second, the local stress $\Delta\sigma$ and the responding stress range Δe are estimated by using the parameters of M_1 mm in Equation (2), taking $\Delta\varepsilon$ and ΔS as input respectively. Finally, the K_f at the same applied strain range can be obtained, and the results are shown in Fig. 10. K_f is not constant but rather a varying value, and it increases at lower applied strain ranges. The strain range dependence of K_f responds well to the lifetime difference in strain-life, especially when it comes to the low applied strain range. At the low strain range regime, the fatigue lifetime becomes more sensitive to the surface condition. The local stress concentration induced by the surface roughness leads to the increasing K_f when approaching the lower applied strain range. In our previous work, the tensile behaviour show significant change when the sample thickness goes down to 1 mm [22]. However, the trendline of K_f between AB_1 mm and AB_2 mm do not show much difference, hence, the thin-wall effect does not give great impact on the fatigue behaviour, even though the surface to volume ratio of the AB_1 mm samples is higher.
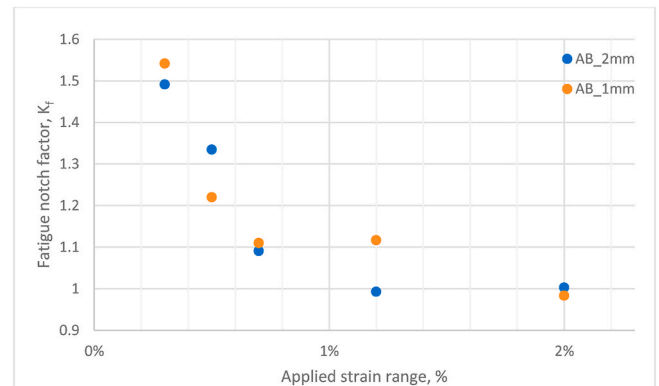

Fig. 10. Calculated fatigue notch factors, K_f, of the tubular specimen with rough as-built surface at different applied strain ranges.

A similar approach of addressing the surface roughness effect has been done by Lee et al. [14], where the K_f is directly derived from the parameters of surface roughness and the radius of valley. The surface texture and material system are similar to this work, but the obtained K_f is a constant value and higher than this work. The reason for the K_f difference is speculated to come from the microstructure at the surface region. In our previous work, a high tensile residual stress is discovered at the surface of the thin-wall structure [22], which indicates a high level of deformation at the surface due to the rapid cooling of PBF-LB. Considering the middle range of SFE of SS 316L [43,46], it is easy to trigger deformation twinning at the surface region. The deformation twins and high level of plastic deformation shown in Fig. 4(c)–(g) are assumed to be beneficial for hindering the crack initiation and propagation. In addition, the great ductility of SS 316L is also expected to lower the stress concentration at the valley of surface roughness at the regime of low applied strain range [17]. In summary, the strain-dependent K_f is majorly related to the surface sensitivity caused by the surface roughness and defects close to the surface area. Meanwhile, the local plasticity indicated by the deformed microstructure at the surface region lowers the overall K_f.

4.3. Cyclic stress response

The comparison of the cyclic stress response between PBF-LB and wrought SS 316L is shown in Fig. 11. Cyclic softening is shown in the PBF-LB SS 316L, but different level of cyclic hardening or softening is shown in the wrought SS 316L. Most importantly, secondary hardening is found in the wrought SS 316L while it is absent in the PBF-LB SS 316L.

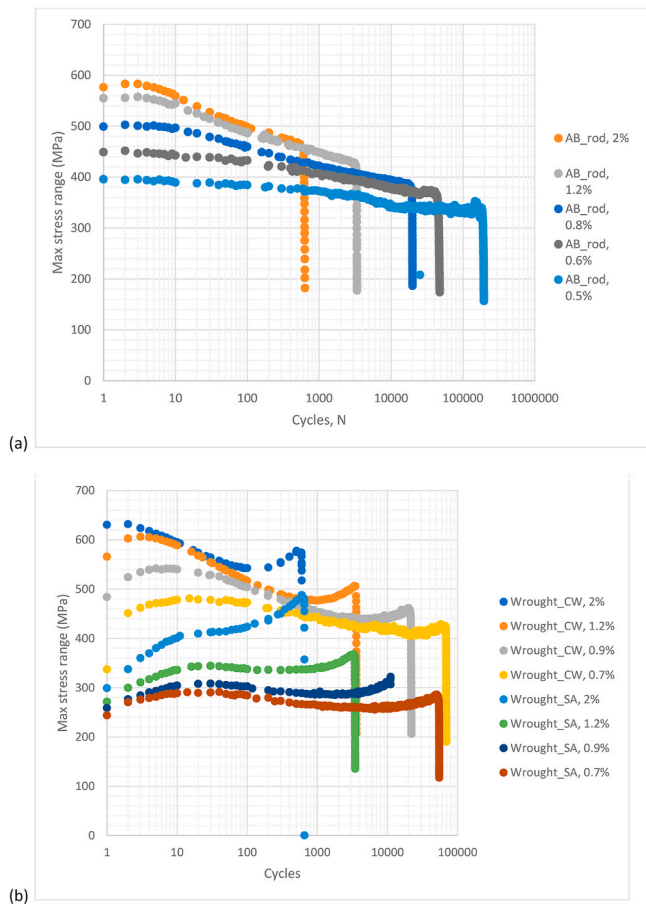The Wrought_CW samples with a high dislocation density shows

cyclic softening, while the Wrought_SA samples with lower dislocation density have a great capacity for cyclic hardening. The cyclic softening/hardening in the beginning followed by continuous softening is commonly found in SS 316L under uniaxial cyclic loading [27,28]. This behaviour correlates to the evolution of the dislocation structure, including the formation of persistent slip band, cell structure, wall structure and labyrinth structure [29–32]. The dislocation rearrangement is highly related to the SFE, where high SFE can lead to cell or wall structure as mentioned above. Low SFE can enhance the dissociation of planar dislocations and increase the possibility of twinning. With a further decrease of SFE, strain-induced martensitic phase transformation can be found in the metastable austenitic stainless steels [57,58]. Considering the middle range SFE of SS 316L, the behaviour typical of both medium and low SFE material might take place. The secondary hardening in LCF caused by martensitic α' transformation has been reported in SS 316L, and it is more pronounced at cryogenic condition [33, 59] or at shear strain loading condition [34]. Although it is uniaxial loading condition at room temperature in this study, the secondary hardening shown in both Wrought_CW and Wrought_SA is assumed to be related to strain-induced martensitic α' transformation since the fatigued samples become magnetic at failure. A higher level of secondary hardening at the higher applied strain ranges is found to be accompanied by a stronger magnetism, which indicates higher level of martensitic α' transformation.

The continuous cyclic softening of the PBF-LB AB_rod samples is expected to be a result of the high dislocation density, the small size of cell structure and the suppressed martensitic α' phase transformation. Due to the rapid cooling of PBF-LB, small size of cell structure (300–500 µm in diameter, see Fig. 5) with high dislocation density is found. The dislocation structure in as-built PBF-LB resembles the cell structure developed in the early cycles in wrought SS316L [35], which refers to a saturated state of dislocation rearrangement. Hence, the cyclic softening comes out as a result of the high dislocation density. However, the fine cell structure in PBF-LB SS 316L is assumed to effectively restrict the dislocation slips, and further hinder the formation of PSB and deformation twins, which are the nucleation sites for martensitic transformation [60]. Therefore, the martensitic α' transformation is possibly suppressed.

In addition, the compositional discrepancy between the wrought and PBF-LB SS 316L leads to the different martensitic α' transformation temperature, M_d. According to Angel [61], M_{d30} refers to the temperature at which 50% of martensite α' is generated after 30% of plastic deformation, and the compositional dependent equation is given as follow,

$$M_{d30}(^\circ C) = 413 - 13.7Cr - 9.5Ni - 8.1Mn - 18.5Mo - 9.2Si - 462(C+N)$$

(4)

where each element is given as wt%. The calculated M_{d30} is $-0.35\,^\circ C$ for the wrought SS 316L, and $-50.23\,^\circ C$ for the PBF-LB SS 316L. The much lower M_{d30} of PBF-LB SS 316L significantly suppresses the martensitic transformation compared to the wrought SS 316L in the test condition of this study. The contribution of each element to the temperature deviation is shown in Table 6. Among the different composition, the divergence of Ni, Mo and Cr plays a big role in the M_{d30}. The composition dependent of M_{d30} actually shares the same perspective with the SFE since the three elements mentioned above have high impact on the SFE [62,63]. Among the three elements, the roughly 3 at% difference of the austenitic phase stabilizer Ni can greatly lift up the SFE, and further lower the TRIP effect. Most importantly, the fatigued samples of PBF-LB SS 316L do not become magnetic, which is a direct evidence that deformation induced martensitic α' is suppressed. However, both the composition difference and fine cell structure are assumed to cause the suppressed martensitic α' transformation, but the contribution of the two mechanisms cannot be deconvoluted in this study.

The dislocation structure of the PBF-LB specimen fatigued to failure

Fig. 11. Cyclic stress response at different applied strain ranges. Note that the cycle is in log scale. (a) PBF-LB AB_rod. (b) Wrought_CW and Wrought_SA.

Table 6

The compositions of elements in PBF-LB and wrought SS 316L that influence the martensitic transformation temperature, M_{d30}, and the contribution of each element to the temperature difference.

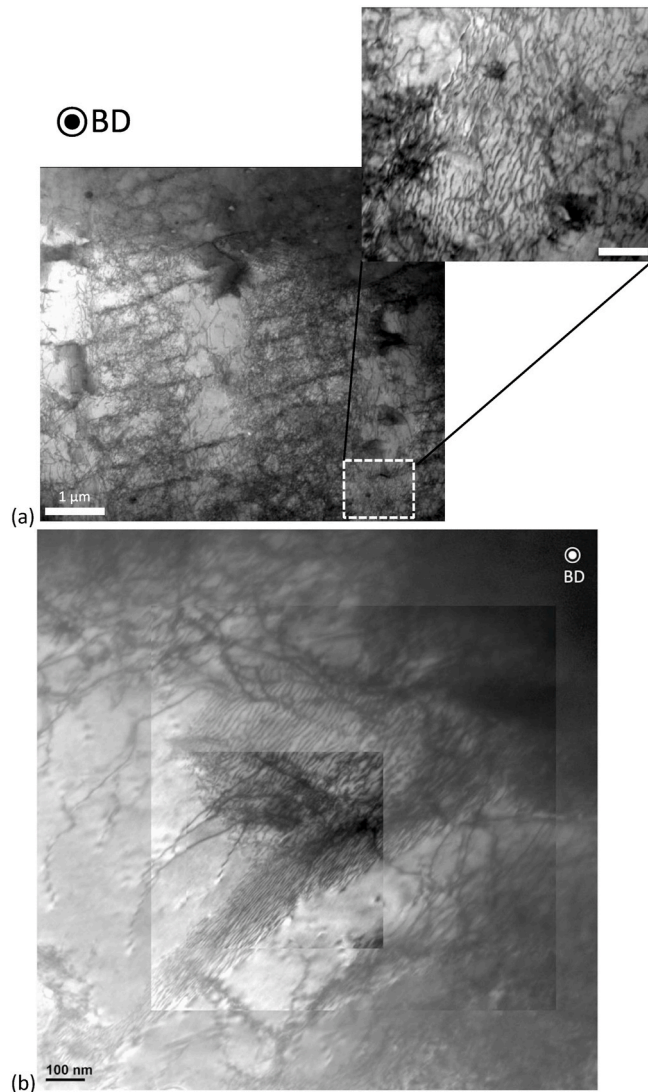|	Cr	Ni	Mn	Mo	Si	C	N
wt% in PBF-LB	17.4	13.4	1.6	2.7	0.3	0.009	0.06
Wt% in Wrought	16.87	10.16	1.51	2.04	0.47	0.01	0.058
ΔT (°C)	−7.261	−30.78	−0.729	−12.21	1.564	0.462	−0.924

Fig. 12. Dislocation structure of AB_rod that is fatigued at failure with the strain range of 0.5%.

is shown in Fig. 12. Dislocation wall structure is found in Fig. 12(a), and it resembles to the similar dislocation structure in wrought SS 316L developed during the fatigue cycles [35,45,64]. Besides, Fig. 12(b) shows the planar movements of edge dislocations, and the screw dislocations interact with these planar edge dislocations. These dislocation movements indicate the unpinning process from the cell boundaries, and they are assumed to be responsible for the cyclic softening behaviour.

5. Conclusion

For the purpose of studying the thin-wall effects in fatigue of PBF-LB SS 316L, tubular specimens were applied to avoid possible buckling in fully reversed fatigue tests. Strain-controlled fatigue testing at room temperature were carried out on three groups of PBF-LB SS 316L with different geometry and surface condition, and they are compared to two groups of wrought SS 316L. The conclusions are drawn as below:

1. Higher level of deformation is found at the surface region of the as-built PBF-LB microstructure, and it is assumed to be caused by the surface tension and rapid cooling during the PBF-LB process. Furthermore, deformation induced twins are shown close to the surface region.
2. The PBF-LB process results in high roughness of the as-built surface, and the roughness of 1 mm samples are slightly higher than for 2 mm samples. In addition, the roughness of the inner surface is found to be much higher than at the outer surface, which is due to that more powder is stacking on each other caused by higher heat accumulation. However, the higher inner surface roughness does not enlarge the valley of roughness profile and the stress concentration effect.
3. For the strain-life fatigue results, the lifetime difference between the as-built and the machined surfaces becomes larger at the lower applied strain ranges, which is due to the increasing sensitivity to stress concentrations. If the surface roughness of the as-built component is evaluated as micro-notches, the effective fatigue notch factor K_f is found to be in reverse relation with the applied strain range. The strain-dependent K_f is majorly related to the surface sensitivity caused by the surface roughness and defects close to the surface area. Meanwhile, the local plasticity at surface region lowers the overall K_f. The surface sensitivity in the fatigue behaviour is also indicated by the lifetime difference between the tubular and cylindrical specimens machined samples. Yet, no significant difference in mechanical behaviour or microstructure between 1 mm and 2 mm specimens were found.
4. For the corresponding stress-life, the fatigue strength is in the following order, Wrought_CW > PBF-LB > Wrought_SA. Cyclic softening is shown for the PBF-LB SS 316L, which is different from the cyclic stress response of initial and secondary hardening of the wrought SS 316L. The secondary hardening in the wrought SS 316L is caused by the deformation induced martensitic α' phase transformation. Meanwhile, the transformation in the PBF-LB SS 316L is suppressed by the cell structure and the lower M_{d30} value. During cycling of PBF-LB SS 316L, the dislocations undergo unpinning from the cell boundaries and planar movement, which results in cyclic softening.

CRediT authorship contribution statement

Cheng-Han Yu: Conceptualization, Methodology, Validation, Investigation, Data curation, Writing – original draft, Writing – review & editing, Visualization, Project administration. **Alexander Leicht:** Validation, Investigation, Writing – review & editing. **Ru Lin Peng:** Writing – review & editing, Supervision. **Johan Moverare:** Conceptualization, Methodology, Writing – review & editing, Supervision, Funding acquisition.

Declaration of competing interest

The authors declare that they have no known competing financial interests or personal relationships that could have appeared to influence the work reported in this paper.

References

[1] B.K. Nagesha, V. Dhinakaran, M. Varsha Shree, K.P. Manoj Kumar, D. Chalawadi, T. Sathish, Review on characterization and impacts of the lattice structure in additive manufacturing, in: Materials Today: Proceedings, 2020.

[2] L. Chougrani, J.P. Pernot, P. Véron, S. Abed, Lattice structure lightweight triangulation for additive manufacturing, CAD Comput. Aided Des. 90 (2017) 95–104.

[3] M.S. Shinde, K.M. Ashtankar, Additive manufacturing-assisted conformal cooling channels in mold manufacturing processes, Adv. Mech. Eng. 9 (5) (2017).

[4] L.E. Rannar, A. Glad, C.G. Gustafson, Efficient cooling with tool inserts manufactured by electron beam melting, Rapid Prototyp. J. 13 (3) (2007).

[5] O. Andersson, A. Graichen, H. Brodin, V. Navrotsky, Developing additive manufacturing technology for burner repair, J. Eng. Gas Turbines Power 139 (3) (2016), 031506.

[6] T. DebRoy, et al., "Additive manufacturing of metallic components – process, structure and properties, Prog. Mater. Sci. 92 (2018) 112–224.

[7] C.Y. Yap, et al., Review of selective laser melting: materials and applications, Appl. Phys. Rev. 2 (4) (2015).

[8] D. Bourell, et al., Materials for additive manufacturing, CIRP Ann. - Manuf. Technol. 66 (2) (2017) 659–681.

[9] D. Herzog, V. Seyda, E. Wycisk, C. Emmelmann, Additive manufacturing of metals, Acta Mater. 117 (2016) 371–392.

[10] M. Kahlin, H. Ansell, J.J. Moverare, Fatigue behaviour of notched additive manufactured Ti6Al4V with as-built surfaces, Int. J. Fatig. 101 (2017) 51–60.

[11] M. Kahlin, et al., Improved fatigue strength of additively manufactured Ti6Al4V by surface post processing, Int. J. Fatig. 134 (2020) 105497. January.

[12] A. Yadollahi, N. Shamsaei, Additive manufacturing of fatigue resistant materials: challenges and opportunities, Int. J. Fatig. 98 (2017) 14–31.

[13] N.E. Dowling, Mechanical Behavior of Materials: Engineering Methods for Deformation, Fracture, and Fatigue, Pearson, 2012.

[14] S. Lee, J.W. Pegues, N. Shamsaei, Fatigue behavior and modeling for additive manufactured 304L stainless steel: the effect of surface roughness, Int. J. Fatig. 141 (2020) 105856.

[15] H. Neuber, Theory of Notch Stresses: Principles for Exact Calculation of Strength with Reference to Structural Form and Material, 1958.

[16] D. Arola, C.L. Williams, Estimating the fatigue stress concentration factor of machined surfaces, Int. J. Fatig. 24 (9) (2002) 923–930.

[17] S. Leuders, T. Lieneke, S. Lammers, T. Tröster, T. Niendorf, On the fatigue properties of metals manufactured by selective laser melting - the role of ductility, J. Mater. Res. 29 (17) (2014) 1911–1919.

[18] R. Shrestha, J. Simsiriwong, N. Shamsaei, Fatigue Behavior of Additive Manufactured 316L Stainless Steel Parts: Effects of Layer Orientation and Surface Roughness, *Addit. Manuf.*, 2019.

[19] B. Blinn, M. Klein, C. Gläßner, M. Smaga, J.C. Aurich, T. Beck, An investigation of the microstructure and fatigue behavior of additively manufactured AISI 316L stainless steel with regard to the influence of heat treatment, Metals 8 (4) (2018) 220.

[20] V.P. Sabelkin, G.R. Cobb, B.M. Doane, R.A. Kemnitz, R.P. O'Hara, Torsional behavior of additively manufactured nickel alloy 718 under monotonic loading and low cycle fatigue, Mater. Today Commun. 24 (2020) 101256.

[21] M. Zhang, C.N. Sun, X. Zhang, J. Wei, D. Hardacre, H. Li, High cycle fatigue and ratcheting interaction of laser powder bed fusion stainless steel 316L: fracture behaviour and stress-based modelling, Int. J. Fatig. 121 (2019) 252–264.

[22] C.H. Yu, et al., Thin-wall effects and anisotropic deformation mechanisms of an additively manufactured Ni-based superalloy, Addit. Manuf. 36 (2020) 101672.

[23] Y.M. Wang, et al., Additively manufactured hierarchical stainless steels with high strength and ductility, Nat. Mater. 17 (1) (2018) 63–70.

[24] D. Kong, et al., About metastable cellular structure in additively manufactured austenitic stainless steels, Addit. Manuf. 38 (2021) 101804. December 2020.

[25] L. Cui, S. Jiang, J. Xu, R.L. Peng, R.T. Mousavian, J. Moverare, Revealing relationships between microstructure and hardening nature of additively manufactured 316L stainless steel, Mater. Des. 198 (2021) 109385.

[26] C.-H. Yu, R.L. Peng, H. Brodin, J. Moverare, Anisotropic deformation and fracture mechanisms of an additively manufactured Ni-based superalloy. In *TMS Superalloys 2020*, 2020, pp. 1003–1013.

[27] R. Alain, P. Violan, J. Mendez, Low cycle fatigue behavior in vacuum of a 316L type austenitic stainless steel between 20 and 600°C part I: fatigue resistance and cyclic behavior, Mater. Sci. Eng. A 229 (1–2) (1997) 87–94.

[28] K. Obrtlík, T. Kruml, J. Polák, Dislocation structures in 316L stainless steel cycled with plastic strain amplitudes over a wide interval, Mater. Sci. Eng. A 187 (1) (1994) 1–9.

[29] T. Kruml, J. Polák, K. Obrtlík, S. Degallaix, Dislocation structures in the bands of localised cyclic plastic strain in austenitic 316L and austenitic-ferritic duplex stainless steels, Acta Mater. 45 (12) (1997) 5145–5151.

[30] J. Polák, et al., The role of extrusions and intrusions in fatigue crack initiation, Eng. Fract. Mech. 185 (2017) 46–60.

[31] P. Spätig, M. Heczko, T. Kruml, H.P. Seifert, Influence of mean stress and light water reactor environment on fatigue life and dislocation microstructures of 316L austenitic steel, J. Nucl. Mater. 509 (2018) 15–28.

[32] M. Gerland, R. Alain, B. Ait Saadi, J. Mendez, Low cycle fatigue behaviour in vacuum of a 316L-type austenitic stainless steel between 20 and 600°C - Part II: dislocation structure evolution and correlation with cyclic behaviour, Mater. Sci. Eng. A 229 (1–2) (1997) 68–86.

[33] Y.C. Jeon, C.S. Kim, H. Ki, S.I. Kwun, J.W. Byeon, Strain-induced martensitic phase transformation by low-cycle fatigue in AISI 316L stainless steel, Mater. Sci. Forum 580 (582) (2008) 597–600.

[34] V. Mazánová, M. Heczko, V. Škorík, A. Chlupová, J. Polák, T. Kruml, Microstructure and martensitic transformation in 316L austenitic steel during multiaxial low cycle fatigue at room temperature, Mater. Sci. Eng., A 767 (September) (2019).

[35] M.S. Pham, C. Solenthaler, K.G.F. Janssens, S.R. Holdsworth, Dislocation structure evolution and its effects on cyclic deformation response of AISI 316L stainless steel, Mater. Sci. Eng., A 528 (7–8) (2011) 3261–3269.

[36] W.F. Hosford, Mechanical Behavior of Materials, 2005.

[37] I. Karaman, H. Sehitoglu, Y.I. Chumlyakov, H.J. Maier, The Deformation of Low-Stacking-Fault-Energy Austenitic Steels, *JOM*, 2002.

[38] S. Vercammen, B. Blanpain, B.C. De Cooman, P. Wollants, Cold rolling behaviour of an austenitic Fe-30Mn-3Al-3Si TWIP-steel: the importance of deformation twinning, Acta Mater. 52 (7) (2004) 2005–2012.

[39] D. Barbier, N. Gey, S. Allain, N. Bozzolo, M. Humbert, Analysis of the tensile behavior of a TWIP steel based on the texture and microstructure evolutions, Mater. Sci. Eng. A 500 (1–2) (2009) 196–206.

[40] S. Zaefferer, J. Ohlert, W. Bleck, A study of microstructure, transformation mechanisms and correlation between microstructure and mechanical properties of a low alloyed TRIP steel, Acta Mater. 52 (9) (2004) 2765–2778.

[41] C. Herrera, D. Ponge, D. Raabe, Design of a novel Mn-based 1 GPa duplex stainless TRIP steel with 60% ductility by a reduction of austenite stability, Acta Mater. 59 (11) (2011) 4653–4664.

[42] M.A. Meyers, et al., Dependence of tensile deformation behavior of TWIP steels on stacking fault energy, temperature and strain rate, Acta Mater. 60 (6) (2009) 2135–2145.

[43] J. Lu, et al., Stacking fault energies in austenitic stainless steels, Acta Mater. 111 (2016) 39–46. June.

[44] S.Y. Zhang, E. Compagnon, B. Godin, A.M. Korsunsky, Investigation of martensite transformation in 316L stainless steel, Mater. Today Proc. 2 (2015) S251–S260.

[45] J. Man, et al., Stability of austenitic 316L steel against martensite formation during cyclic straining, Procedia Eng. 10 (2011) 1279–1284.

[46] W. Woo, et al., stacking fault energy analyses of additively manufactured stainless steel 316L and CrCoNi medium entropy alloy using in situ neutron diffraction, Sci. Rep. 10 (1) (2020) 2–4.

[47] M.S. Pham, B. Dovgyy, P.A. Hooper, Twinning induced plasticity in austenitic stainless steel 316L made by additive manufacturing, Mater. Sci. Eng., A 704 (April) (2017) 102–111.

[48] D. Molnár, X. Sun, S. Lu, W. Li, G. Engberg, L. Vitos, Effect of temperature on the stacking fault energy and deformation behaviour in 316L austenitic stainless steel, Mater. Sci. Eng. A 759 (2019) 490–497.

[49] S. Sjöström, R. Eriksson, S. Johansson, H. Brodin, X.-H. Li, L. Östergren, "TBC bond coat–top coat interface roughness: influence on fatigue life and modelling aspects, Surf. Coating. Technol. 236 (2013) 230–238.

[50] S. Suresh, Fatigue of Materials, 1998.

[51] W. Ramberg, W.R. Osgood, Description of stress-strain curves by three parameters, Natl. Advis. Comm. Aeronaut. (902) (1943).

[52] A. Riemer, S. Leuders, M. Thöne, H.A. Richard, T. Tröster, T. Niendorf, On the fatigue crack growth behavior in 316L stainless steel manufactured by selective laser melting, Eng. Fract. Mech. 120 (2014) 15–25.

[53] A. Leicht, C.-H. Yu, V. Luzin, U. Klement, E. Hryha, Effect of scan rotation on the microstructure development and mechanical properties of 316L parts produced by laser powder bed fusion, Mater. Char. 163 (2020) 110309.

[54] D. Ma, A.D. Stoica, Z. Wang, A.M. Beese, Crystallographic texture in an additively manufactured nickel-base superalloy, Mater. Sci. Eng., A 684 (2017) 47–53. September 2016.

[55] D. Deng, R.L. Peng, H. Brodin, J. Moverare, Microstructure and mechanical properties of Inconel 718 produced by selective laser melting: sample orientation dependence and effects of post heat treatments, Mater. Sci. Eng., A 713 (2018) 294–306. December 2017.

[56] "Peterson's Stress Concentration Factors," *Choice Rev. Online*, 1998.

[57] P. Mangonon, G. Thomas, Martensite phases IN 304 stainless steel, Metall. Trans. 1 (1970) 1577–1586.

[58] J.A. Venables, The martensite transformation in stainless steel, Philos. Mag. A 7 (73) (1962) 35–44.

[59] J.B. Vogt, J. Foct, C. Regnard, G. Robert, J. Dhers, Low-temperature fatigue of 316 and 316LN austenitic stainless steels, Metall. Trans. A 22 (10) (1991) 2385–2392.

[60] Y. Hong, et al., Formation of strain-induced martensite in selective laser melting austenitic stainless steel, Mater. Sci. Eng., A 740–741 (2019) 420–426. October 2018.

[61] T. Angel, formation of martensite in austenitic stainless steels, J. Iron Steel Inst. 177 (1954) 165–174.

[62] C.G. Rhodes, A.W. Thompson, The composition dependence of stacking fault energy in austenitic stainless steels, Metall. Trans. A 8 (12) (1977) 1901–1906.

[63] R.E. Schramm, R.P. Reed, Stacking fault energies of seven commercial austenitic stainless steels, Metall. Trans. A 6 (7) (1975) 1345.

[64] T. Mayama, K. Sasaki, M. Kuroda, Quantitative evaluations for strain amplitude dependent organization of dislocation structures due to cyclic plasticity in austenitic stainless steel 316L, Acta Mater. 56 (12) (2008) 2735–2743.